Hindawi
Shock and Vibration
Volume 2021, Article ID 5511817, 15 pages
https://doi.org/10.1155/2021/5511817

Research Article

Investigation of Dynamic Load Sharing Behavior for Herringbone Planetary Gears considering Multicoupling Manufacturing Errors

Fei Ren,[1] **Jinchen Ji**,[2] **Guofu Luo**,[1] **Shaofu Zhao**,[3] **Liya Zhao**,[2] **Guiqin Shi**,[4] **Xiaoling Wu**,[5] **and Ning Wang**[6]

[1]*School of Mechanical and Electrical Engineering & Henan Key Laboratory of Intelligent Manufacturing of Mechanical Equipment, Zhengzhou University of Light Industry, Zhengzhou 450002, China*
[2]*School of Mechanical and Mechatronic Engineering, Faculty of Engineering and Information Technology, University of Technology Sydney, Broadway, NSW 2007, Australia*
[3]*Zhengzhou Research Institute of Mechanical Engineering Co., Ltd., Zhengzhou 450001, China*
[4]*Zhengzhou University of Light Industry, Zhengzhou 450002, China*
[5]*State Key Laboratory of Mechanical Transmission, Chongqing University, Chongqing 400044, China*
[6]*Underground Space Design and Research Institute, China Railway Engineering Equipment Group Co. Ltd., Zhengzhou 450016, China*

Correspondence should be addressed to Fei Ren; renfei2015@zzuli.edu.cn

Received 25 February 2021; Revised 23 June 2021; Accepted 1 July 2021; Published 10 July 2021

Academic Editor: Francesco Pellicano

Copyright © 2021 Fei Ren et al. This is an open access article distributed under the Creative Commons Attribution License, which permits unrestricted use, distribution, and reproduction in any medium, provided the original work is properly cited.

In this study, based on the lumped-parameter theory and the Lagrange approach, a novel and generalized bending-torsional-axial coupled dynamic model for analyzing the load sharing behavior in the herringbone planetary gear train (HPGT) is presented by taking into account the actual structure of herringbone gears, manufacturing errors, time-dependent meshing stiffness, bearing deflections, and gyroscopic effects. The model can be applied to the analysis of the vibration of the HPGT with any number of planets and different types of manufacturing errors in different floating forms. The HPGT equivalent meshing error is analyzed and derived for the tooth profile errors and manufacturing eccentric errors of all components in the HPGT system. By employing the variable-step Runge–Kutta approach to calculate the system dynamic response, in conjunction with the presented calculation approach of the HPGT load sharing coefficient, the relationships among manufacturing errors, component floating, and load sharing are numerically obtained. The effects of the combined errors and single error on the load sharing are, respectively, discussed. Meanwhile, the effects of the support stiffness of the main components in the HPGT system on load sharing behavior are analyzed. The results indicate that manufacturing errors, floating components, and system support stiffness largely influence the load sharing behavior of the HPGT system. The research has a vital guiding significance for the design of the HPGT system.

1. Introduction

Herringbone planetary gear train (HPGT) possesses the advantages in power split, compact structure, large transmission ratio, high transmission efficiency, strong carrying capacity, and small axial force, and thus it has been widely applied in the transmission systems of wind turbines, nuclear power plants, aircrafts, ships, and vehicles. However, in the presence of the inevitable manufacturing errors, elastic deformations, and so on, the HPGT cannot achieve the uniform load distribution among different transmission paths. On the one hand, this would lose the advantages of herringbone planetary transmission, and on the other hand, this would lead to overload, vibration, and noise of some components, which affect the service life, stability, and reliability of the gear set [1]. Consequently, it is of practical

significance to construct a refined dynamic load sharing model of herringbone planetary gears to develop an in-depth understanding of load distribution characteristics resulting from the inevitable manufacturing errors.

Some studies were devoted to investigating the dynamic behavior and load sharing of the planetary gear train (PGT). Lin and Parker established a spur PGT dynamic model to analyze its modal properties [2, 3]. Zhao and Ji developed a torsional dynamic model of the multistage spur PGTs of a wind turbine gearbox for the analysis of its nonlinear dynamic characteristics [4]. Zhang and Zhu investigated the planet meshing phase effect on load sharing characteristics of herringbone gear transmission system [5]. Mo et al. studied the load distribution behavior of compound planetary powertrains applied in wind turbine gearbox [6]. Singh developed the load sharing behavior analysis model of planetary gear transmission [7, 8]. Ligata et al. [9] and Bodas and Kahraman [10] examined the static load sharing behaviors of the planetary transmission. Zhu and Xu researched the impact of flexible pin shaft stiffness on load sharing features of planetary gearbox used in wind turbines [11]. Ren et al. investigated the effects of manufacturing errors on the dynamic behaviors and floating characteristics of herringbone planetary gears [1, 12, 13]. Li et al. conducted the analysis of load sharing and reliability prediction of helicopter planetary gear transmission [14]. Kang and Kahraman presented the dynamic features of the double-helical gear pair adopting theoretical and experimental methods [15]. Sondkar and Kahraman studied the dynamics of double-helical planetary gears [16].

Despite the extensive investigations on the PGT dynamics, there is little research on the effects of multicoupling manufacturing errors and system stiffness on the load sharing behavior of the HPGT system. Meanwhile, the presence of multicoupling manufacturing errors can induce the axial dynamic force for the HPGT system. Therefore, the axial degree of freedom (DOF) of each component needs to be considered in the HPGT dynamic modeling. In addition, the HPGT system has its own specific characteristics. Specifically, due to the assembly limitations, the internal ring gear needs to adopt two separate helical gears. As a result, there are the characteristics of both helical and herringbone gears on both sides in HPGT. Thus, these specific characteristics should be considered in the dynamic modeling of the HPGT system.

Meanwhile, the load sharing coefficient is one of the key design parameters of the HPGT system, whose reasonable selection noticeably affects its dynamic characteristics. In the past, the load sharing coefficient was chosen in terms of the empirical value in the design manual, whereas in this paper, a refined HPGT dynamic model will be proposed to calculate the HPGT load sharing coefficient more accurately. It is expected that this research provides an alternative and novel methodology for accurately selecting the load sharing coefficient and thus has important scientific and engineering significances in applications.

In this paper, based on the structure features of herringbone gears, a novel refined dynamic load sharing model for the HPGT considering manufacturing errors is presented by using the lumped-parameter method. The load sharing behavior of an example HPGT is numerically simulated, and the effects of manufacturing errors and system support stiffness on the dynamic load sharing behavior are analyzed.

2. Composition and Operation Principle of the HPGT System

Figure 1 shows the structural and kinematic diagram of herringbone planetary gear transmissions, which comprises a herringbone sun gear, two ring gears (i.e., left and right ring gears), N herringbone planet gears, and a carrier. As demonstrated in Figure 1, the symbols s, $r2$, $r1$, p_i, and c indicate the sun gear, ring gears, planet gear, and carrier, respectively. The sun gear s is taken as the input component, carrier c is taken as the output member, and the two ring gears are taken as the stationary components. By considering assembly, the ring gear adopts two helical gears with contrary helix angles. In the HPGT system, there are two kinds of meshing pairs, namely, internal mesh (i.e., planet-left ring mesh and planet-right ring mesh) and external mesh (i.e., sun-planet mesh).

3. Dynamic Model of the HPGT System

3.1. Dynamic Model. Figure 2 shows the three-dimensional (3D) bending-torsional-axial coupled dynamic model for the HPGT system in consideration of both sides of herringbone gears and the axial DOF of each component, which differentiate the developed dynamic model from the existing models of two-dimensional (2D) PGT. For the sake of simplicity, only one planet gear is displayed in Figure 2. The floating component is represented by the low radial support stiffness. In the previous investigations on herringbone gears, it was assumed that the axial forces between two helical gears with opposite rotation directions canceled each other. Accordingly, the axial vibration was ignored and the herringbone gear was simplified to a 2D plane model. As a matter of fact, since there exist manufacturing errors, the dynamic performance of left and right gear pairs cannot be identical. To more accurately demonstrate the dynamic behaviors of herringbone gears, the actual structural properties of herringbone gears on both sides, the axial vibrations of the central member, and each planet are considered in the present dynamic model as depicted in Figure 2. In assembly, the ring gear utilizes two helical gears with the opposite helix angles. Consequently, each component (i.e., sun gear, left and right ring gears, carrier, and each planet gear) has four DOFs including one rotation and three translations, which are denoted as x_j, y_j, z_j, θ_j, $j = s, r2, r1, c$ and ξ_i, η_i, ρ_i, θ_i, $i = 1, 2, \ldots, N$, respectively. The frames of reference are illustrated in detail in Figures 2–5, where the superscripts R and L indicate the right and left sides of the component, respectively. In order to facilitate the calculation, each angular displacement θ is converted into an equivalent linear displacement u in the tangential direction of the corresponding base circle:

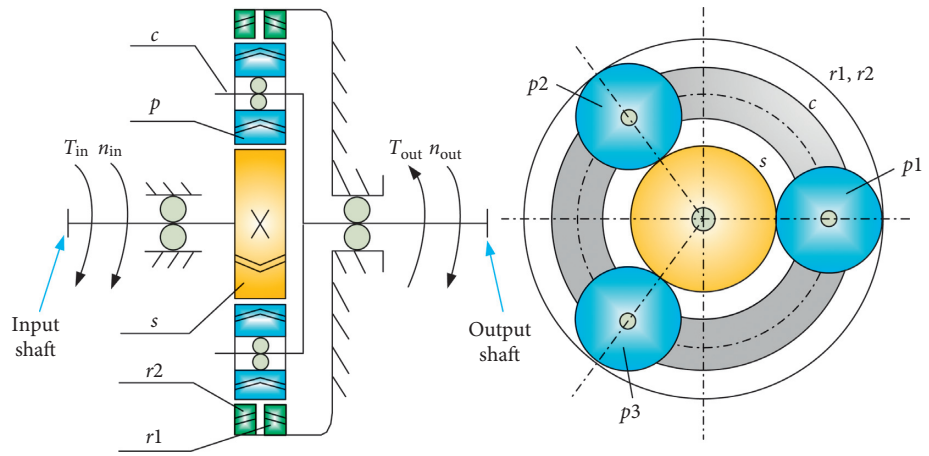

FIGURE 1: Kinematic sketch of herringbone planetary gears.

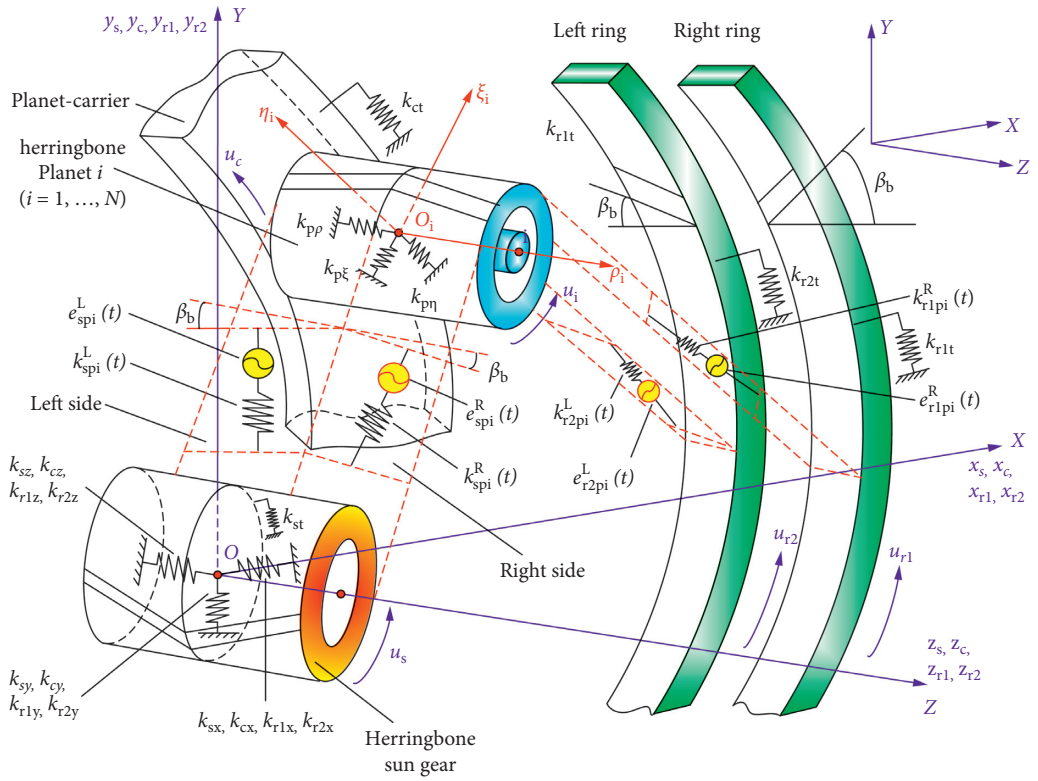

FIGURE 2: The refined coupled dynamic model of the HPGT system.

$$\begin{cases} u_s = r_s \cdot \theta_s, \\ u_{r2} = r_{r2} \cdot \theta_{r2}, \\ u_{r1} = r_{r1} \cdot \theta_{r1}, \\ u_c = r_c \cdot \theta_c, \\ u_i = r_i \cdot \theta_i, \quad i = 1, 2, \ldots, N, \end{cases} \tag{1}$$

where r_s, r_{r2}, r_{r1}, r_i are, respectively, the base circle radius of the sun gear, left and right ring gears, and the ith planet gear, while r_c is the distance from the carrier rotation center to the planet gear center. Hence, there are a total of $16 + 4N$ DOFs in the proposed model shown in Figure 2. They can be expressed as

$$\mathbf{U} = \{\mathbf{U}_c, \mathbf{U}_{r2}, \mathbf{U}_{r1}, \mathbf{U}_s, \mathbf{U}_1, \mathbf{U}_2, \ldots, \mathbf{U}_N\}^T, \tag{2}$$

where $\mathbf{U}_c = \{x_c, y_c, z_c, u_c\}^T$, $\mathbf{U}_{r2} = \{x_{r2}, y_{r2}, z_{r2}, u_{r2}\}^T$, $\mathbf{U}_{r1} = \{x_{r1}, y_{r1}, z_{r1}, u_{r1}\}^T$, $\mathbf{U}_s = \{x_s, y_s, z_s, u_s\}^T$, and $\mathbf{U}_i = \{\xi_i, \eta_i, \rho_i, u_i\}^T$ $(i = 1, \cdots, N)$.

In the dynamic load sharing model shown in Figure 2, k_{spi}, k_{r1pi}, and k_{r2pi} are the meshing stiffness for the ith sun-planet pair, right ring-planet pair, and left ring-planet pair, respectively. k_s, k_c, k_{r1}, k_{r2}, and k_p are the bearing support stiffness of the sun gear, carrier, right and left ring gears, and

planet gear, respectively. k_t is the torsional support stiffness. Here, the subscript *spi* stands for sun-planet gear *i* pair, the subscript *r*1*pi* indicates right ring-planet gear *i* pair, and the subscript *r*2*pi* represents left ring-planet gear *i* pair. The symbol *pi* denotes the *i*th planet gear, and symbols *s*, *c*, *r*2, and *r*1 are of the same meanings as those demonstrated in Figure 1.

According to the presented HPGT dynamic model in Figure 2, the equivalent displacements of the *i*th planet-sun gear mesh, the *i*th planet-left (right) ring gear mesh, and the *i*th planet-carrier pair can be derived as [12, 17, 18]

$$\begin{aligned}
\mu_{spi}^{L(R)} &= -x_s \sin\phi_{si} \cdot \cos\beta_b + y_s \cos\phi_{si} \cdot \cos\beta_b + z_s \cdot \sin(\pm\beta_b) + u_s \cdot \cos\beta_b - \xi_i \sin\alpha_t \cdot \cos\beta_b - \eta_i \cos\alpha_t \cdot \\
&\quad \cos\beta_b - \rho_i \cdot \sin(\pm\beta_b) + u_i \cdot \cos\beta_b + e_{spi}^{L(R)}(t), \\
\mu_{r2(1)pi}^{L(R)} &= -x_{r2(1)} \sin\phi_{ri} \cdot \cos\beta_b + y_{r2(1)} \cos\phi_{ri} \cdot \cos\beta_b - z_{r2(1)} \cdot \sin(\pm\beta_b) + u_{r2(1)} \cdot \cos\beta_b + \xi_i \sin\alpha_t \cdot \\
&\quad \cos\beta_b - \eta_i \cos\alpha_t \cdot \cos\beta_b + \rho_i \cdot \sin(\pm\beta_b) - u_i \cdot \cos\beta_b + e_{r2(1)pi}^{L(R)}(t), \\
&\begin{cases}
\mu^{\xi cpi} = -\xi_i + x_c \cdot \cos\phi_i + y_c \cdot \sin\phi_i, \\
\mu^{\eta cpi} = -\eta_i - x_c \cdot \sin\phi_i + y_c \cdot \cos\phi_i + u_c, \\
\mu_{\rho cpi} = \rho_i - z_c,
\end{cases}
\end{aligned} \tag{3}$$

where $\mu_{spi}^{L(R)}$ indicates the equivalent microdeformation of the *i*th planet-sun gear pair on the left (right) side. $\mu_{r2(1)pi}^{L(R)}$ indicates the equivalent microdeformation of the *i*th planet-left (right) ring gear pair. $\mu^{\xi cpi}$, $\mu^{\eta cpi}$, $\mu_{\rho cpi}$ are the relative deformations in the ξ-, η-, and ρ-directions of the *i*th carrier-planet pair, respectively. $e_{spi}^{L(R)}(t)$ represents the static transmission error of the *i*th planet-sun gear pair on the left (right) side. $e_{r2(1)pi}^{L(R)}(t)$ represents the static transmission error of the *i*th planet-left (right) ring gear pair. Here, "+" refers to the left-side sun-planet gear *i* pair (left ring-planet gear *i* pair) and "–" for the right-side sun-planet gear *i* pair (right ring-planet gear *i* pair) in symbol "±." β_b expresses the base helix angle. $\phi_{si} = \phi_i - \alpha_t$, $\phi_{ri} = \phi_i + \alpha_t$, where ϕ_i denotes the *i*th planet assembly position angle and α_t stands for the transverse pressure angle.

The meshing forces can be expressed as

$$\begin{cases}
F_{r2piL} = k_{r2pi}^{L} \cdot \mu_{r2pi}^{L}, \\
F_{r2piL} = k_{r1pi}^{R} \cdot \mu_{r1pi}^{R}, \\
F_{spiL} = k_{spi}^{L} \cdot \mu_{spi}^{L}, \\
F_{spiR} = k_{spi}^{R} \cdot \mu_{spi}^{R},
\end{cases} \tag{4}$$

where F_{spiL} and F_{spiR} are the meshing forces for the *i*th planet-sun gear pair on the left side and right side, respectively. F_{r2piL} and F_{r2spil} are the meshing forces of the *i*th planet-left and right ring gear pair, respectively.

3.2. Equations of Motion of the HPGT

3.2.1. Equations of Motion for the Herringbone Sun Gear. Figure 3 presents the dynamic model of the *i*th planet-sun gear pair in the HPGT system in isometric view. Based on D'Alembert's principle, the equations of motion for herringbone sun gear can be obtained as

$$\begin{cases}
m_s(\ddot{x}_s - 2\omega_c\dot{y}_s - \omega_c^2 x_s) - \sum_{i=1}^{N}(F_{spiR} + F_{spiL}) \cdot \cos\beta_b \cdot \sin\varphi_{si} + k_{sx} \cdot x_s = 0, \\
m_s(\ddot{y}_s + 2\omega_c\dot{x}_s - \omega_c^2 y_s) + \sum_{i=1}^{N}(F_{spiR} + F_{spiL}) \cdot \cos\beta_b \cdot \cos\varphi_{si} + k_{sy} \cdot y_s = 0, \\
m_s\ddot{z}_s + \sum_{i=1}^{N}(F_{spiR} + F_{spiL}) \cdot \sin\beta_b + k_{sz} \cdot z_s = 0, \\
\left(\frac{J_s}{r_s^2}\right)\ddot{u}_s + \sum_{i=1}^{N}(F_{spiR} + F_{spiL}) \cdot \cos\beta_b + k_{st} \cdot u_s - \frac{T_s}{r_s} = 0,
\end{cases} \tag{5}$$

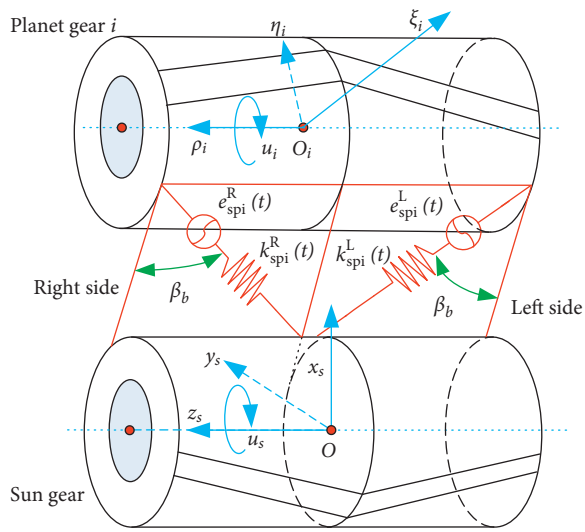

FIGURE 3: Dynamic model of the ith planet-sun gear pair.

where m_s is the sun gear mass; J_s is the sun gear rotational inertia; x_s, y_s, and z_s are the vibration microdisplacements in x-, y-, and z-direction, respectively. u_s is the torsional microdisplacement about z-direction for the sun gear, and T_s indicates the external torque acting on the herringbone sun gear.

3.2.2. Equations of Motion for the Left Helical Ring Gear. Figure 4 presents the dynamic model of the ith left ring- (right ring-) planet gear pair in the HPGT system in isometric view. According to the dynamic model of the internal meshing pair shown in Figure 4 and D'Alembert's principle, the equations of motion for the left ring gear can be written as

$$\begin{cases} m_r\left(\ddot{x}_{r2} - 2\omega_c\dot{y}_{r2} - \omega_c^2 x_{r2}\right)() - \sum_{i=1}^{N} F_{r2piL} \cdot \cos\beta_b \cdot \sin\varphi_{ri} + k_{r2x} \cdot x_{r2} = 0, \\ m_r\left(\ddot{y}_{r2} + 2\omega_c\dot{x}_{r2} - \omega_c^2 y_{r2}\right) + \sum_{i=1}^{N} F_{r2piL} \cdot \cos\beta_b \cdot \cos\varphi_{ri} + k_{r2y} \cdot y_{r2} = 0, \\ m_r z_{r2} + \sum_{i=1}^{N} F_{r2piL} \cdot \sin\beta_b + k_{r2z} \cdot z_{r2} = 0, \\ \left(\frac{J_r}{r_r^2}\right) u_{r2} + \sum_{i=1}^{N} F_{r2piL} \cdot \cos\beta_b + k_{r2t} \cdot u_{r2} = 0, \end{cases} \tag{6}$$

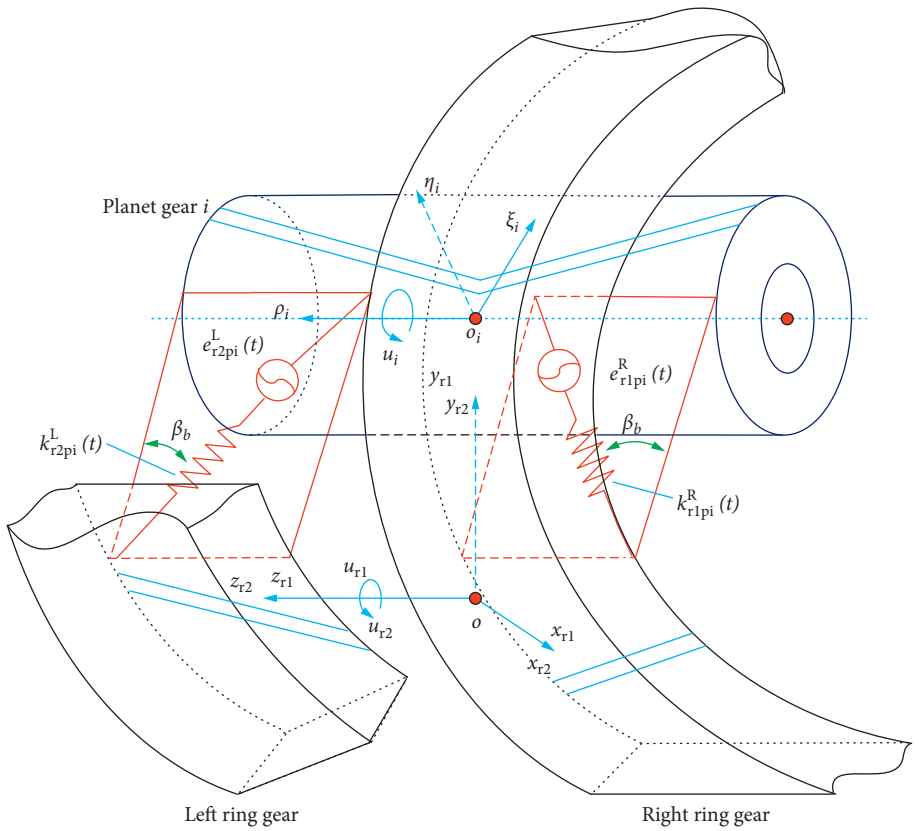

FIGURE 4: Dynamic model of the ith left and right ring-planet gear pairs.

where m_r is the ring gear mass and J_r is the ring gear rotational inertia. x_{r2}, y_{r2}, and z_{r2} are the vibration microdisplacements in x, y, and z directions for the left ring gear, respectively. u_{r2} is the torsional microdisplacement about z-direction for the left ring gear.

3.2.3. Equations of Motion for the Right Helical Ring Gear. The equations of motion for the right ring gear can be deduced as

$$\begin{cases} m_r\left(\ddot{x}_{r1} - 2\omega_c\dot{y}_{r1} - \omega_c^2 x_{r1}\right) - \sum_{i=1}^{N} F_{r1piR}\cdot \cos\beta_b \cdot \sin\varphi_{ri} + k_{r1x}\cdot x_{r1} = 0, \\ m_r\left(\ddot{y}_{r1} + 2\omega_c\dot{x}_{r1} - \omega_c^2 y_{r1}\right) + \sum_{i=1}^{N} F_{r1piR}\cdot \cos\beta_b \cdot \cos\varphi_{ri} + k_{r1y}\cdot y_{r1} = 0, \\ m_r\ddot{z}_{r1} - \sum_{i=1}^{N} F_{r1piR}\cdot \sin\beta_b + k_{r1z}\cdot z_{r1} = 0, \\ \left(\dfrac{J_r}{r_r^2}\right)\ddot{u}_{r1} + \sum_{i=1}^{N} F_{r1piR}\cdot \cos\beta_b + k_{r1t}\cdot u_{r1} = 0, \end{cases} \tag{7}$$

where x_{r1}, y_{r1}, and z_{r1} are, respectively, the vibration microdisplacements in x-, y-, and z-directions for the right ring gear. u_{r1} refers to the torsional microdisplacement about the z-direction for the right ring gear.

3.2.4. Equations of Motion for the Carrier. Figure 5 displays the dynamic model of the ith planet-carrier pair in the HPGT system. By applying D'Alembert's principle, the equations of motion for the carrier can be obtained as

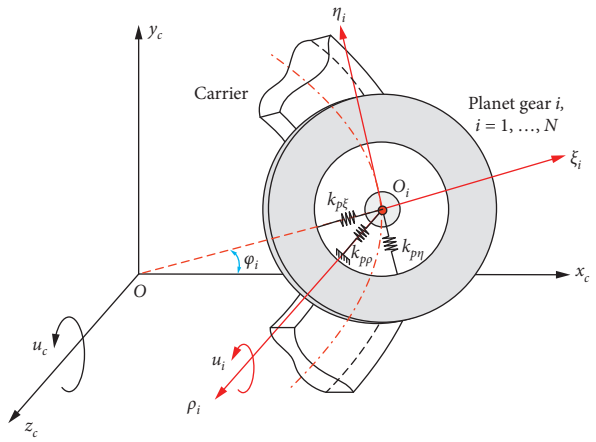

Figure 5: Dynamic model of the ith planet-carrier pair.

$$\begin{cases} m_c\left(\ddot{x}_c - 2\omega_c\dot{y}_c - \omega_c^2 x_c\right)\left(\ddot{x}_c - 2\omega_c\dot{y}_c - \omega_c^2 x_c\right) + \sum_{i=1}^{N}\left(k_{p\xi}\cdot\mu_{\xi cpi}\cdot\ \cos\ \varphi_i - k_{p\eta}\cdot\mu_{\eta cpi}\cdot\ \sin\ \varphi_i\right) + k_{cx}\cdot x_c = 0, \\ m_c\left(\ddot{y}_c + 2\omega_c\dot{x}_c - \omega_c^2 y_c\right) + \sum_{i=1}^{N}\left(k_{p\xi}\cdot\mu_{\xi cpi}\cdot\ \sin\ \varphi_i + k_{p\eta}\cdot\mu_{\eta cpi}\cdot\ \cos\ \varphi_i\right) + k_{cy}\cdot y_c = 0, \\ m_c\ddot{z}_c - \sum_{i=1}^{N} k_{p\rho}\mu_{\rho cpi} + k_{cz}\cdot z_c = 0, \\ \left(\frac{J_c}{r_c^2}\right)\ddot{u}_c + \sum_{i=1}^{N} k_{p\eta}\mu_{\eta cpi} + k_{ct}\cdot u_c + \frac{T_c}{r} = 0, \end{cases} \tag{8}$$

where m_c is the carrier mass; J_c is the carrier rotational inertia; and x_c, y_c, and z_c are the vibration microdisplacements in the x-, y-, and z-direction for the carrier. u_c is the torsional microdisplacement about the z-direction for the carrier. T_c refers to the load torque acting on the carrier.

3.2.5. Equations of Motion for the ith Herringbone Planet Gear. According to Figures 2–5, the equations of motion for the ith herringbone planet gear can be given by

$$\begin{cases} m_p\left(\ddot{\xi}_i - 2\omega_c\dot{\eta}_i - \omega_c^2\xi_i\right) - \left(F_{spiR} + F_{spiL}\right)\cdot\ \sin\ \alpha_t\cdot\ \cos\ \beta_b + \left(F_{r1piR} + F_{r2piL}\right)_b\cdot\ \sin\ \alpha_t\cdot\ \cos\ \beta_b - k_{p\xi}\cdot\mu_{\xi cpi} = 0, \\ m_p\left(\ddot{\eta}_i + 2\omega_c\dot{\xi}_i - \omega_c^2\eta_i\right) - \left(F_{spiR} + F_{spiL}\right)\cdot\ \cos\ \beta_b\cos\ \alpha_t - \left(F_{r1piR} + F_{r2piL}\right)\cdot\ \cos\ \beta_b\cdot\ \cos\ \alpha_t - k_{p\eta}\cdot\mu_{\eta cpi} = 0, \\ m_p\ddot{\rho}_i - F_{spiR}\cdot\ \sin\ \beta_b + F_{spiL}\cdot\ \sin\ \beta_b + F_{r1piR}\cdot\ \sin\ \beta_b - F_{r2piL}\cdot\ \sin\ \beta_b + k_{p\rho}\cdot\mu_{\rho cpi} = 0, \\ \left(\frac{J_p}{r_p^2}\right)\ddot{u}_i + \left(F_{spiR} + F_{spiL}\right)\cdot\ \cos\ \beta_b - \left(F_{r1piR} + F_{r2piL}\right)\cdot\ \cos\ \beta_b = 0, \end{cases} \tag{9}$$

where m_p is the planet gear mass and J_p is the planet gear rotational inertia. ξ_i, η_i, and ρ_i mean the vibration microdisplacements in the ξ, η, and ρ directions for the ith herringbone planet gear, respectively. u_i indicates the torsional microdisplacement about the ρ-direction for the sun gear.

By assembling the above equations of motion for each member, the matrix form of herringbone planetary gear transmissions with N planet gears can be written as

$$[\mathbf{M}]\cdot\left\{\ddot{U}(t)\right\} + \boldsymbol{\omega}_c\cdot[\mathbf{G}]\cdot\left\{\dot{U}(t)\right\} + \left([\mathbf{K}_b] + [\mathbf{K}_m(t)] - \boldsymbol{\omega}_c^2\cdot[\mathbf{K}_\Omega]\right)\cdot\{\mathbf{U}(t)\} = \{\mathbf{T}_k\} + \{\mathbf{T}(t)\}, \tag{10}$$

where $\{\mathbf{U}(t)\}$ indicates the generalized displacement column vector, $[\mathbf{M}]$ indicates the generalized inertial matrix, $[\mathbf{K}_b]$ refers to the supporting stiffness matrix, $[\mathbf{K}_m]$ means the time-dependent meshing stiffness matrix, $[\mathbf{G}]$ represents the gyroscopic matrix, $[\mathbf{K}_\Omega]$ denotes the centripetal stiffness matrix, $\{\mathbf{T}_k\}$ expresses the excitation matrix caused by meshing stiffness and manufacturing error, and $\{\mathbf{T}(t)\}$ denotes the vector of external excitation forces.

4. Multicoupling Manufacturing Error Analysis

This study considers the manufacturing eccentric errors for each component (i.e., the carrier and each gear) and tooth profile errors of each gear. These tooth profile errors and eccentric errors are transformed into the line of action (LOA) of the gear pair, respectively, and the equivalent displacements of the errors can be acquired by superposition.

4.1. Equivalent Displacements of Eccentric Errors. Figure 6 illustrates the projection relation of manufacturing eccentric errors for herringbone planetary gear set on the line of action, where E_s and β_s, respectively, represent the manufacturing eccentric error and its initial phase of the sun gear. e refers to the equivalent meshing error on the meshing line. ω denotes the angular velocity of each component. φ_i means the position angle of the ith planet gear, and $\varphi_i = 2\pi(i-1)/N$, where N is the planet number. Here, the subscripts s, $r1$, $r2$, pi, and c have the same meanings as those exhibited in Figure 1. n and w refer to the internal and external mesh, respectively. α is the pressure angle, and $\alpha_n = \alpha_w = \alpha_t$.

In view of Figure 6 and the relative motion state of each component, the equivalent meshing error of sun-gear manufacturing eccentric error and initial phase (E_s, β_s) on the external meshing line can be obtained as

$$e_{Esi} = -E_s \sin\left((\omega_s - \omega_c)t + \beta_s + \alpha_t - \varphi_i\right). \tag{11}$$

Similarly, the equivalent meshing error of planet-gear manufacturing eccentric error and initial phase (E_{pi}, β_{pi}) on the external and internal meshing line can, respectively, be given by

$$\begin{aligned} e_{wEpi} &= -E_{pi} \sin\left(\left(\omega_p - \omega_c\right)t + \beta_{pi} + \alpha_t\right), \\ e_{nEpi} &= E_{pi} \sin\left(\left(\omega_p - \omega_c\right)t + \beta_{pi} + \alpha_t\right). \end{aligned} \tag{12}$$

The equivalent meshing error of left ring-gear manufacturing eccentric error and initial phase (E_{r2}, β_{r2}) on the internal meshing line can be denoted as

$$e_{Er2i} = E_{r2}^L \sin\left(-\omega_c t + \beta_{r2} - \alpha_t - \varphi_i\right). \tag{13}$$

The equivalent meshing error of right ring-gear manufacturing eccentric error and initial phase (E_{r1}, β_{r1}) on the internal meshing line can be derived as

$$e_{Er1i} = E_{r1}^R \sin\left(-\omega_c t + \beta_{r1} - \alpha_t - \varphi_i\right). \tag{14}$$

The equivalent meshing error of carrier manufacturing eccentric error and initial phase (E_c, β_c) on the external and internal meshing line can, respectively, be expressed as

$$\begin{aligned} e_{wEci} &= E_c \sin\left(\beta_c - \varphi_i\right) \cdot \cos\alpha_t, \\ e_{nEci} &= -E_c \sin\left(\beta_c - \varphi_i\right) \cdot \cos\alpha_t. \end{aligned} \tag{15}$$

The equivalent cumulative meshing errors generated by the superposition of the eccentric errors of each component for the internal and external meshing lines on the left and right sides of herringbone planetary gear transmission can, respectively, be expressed as

$$\begin{aligned} eE_{r2pi}^L &= E_{r2}^L \cdot \sin\left(-\omega_c \cdot t + \beta_{r2} - \alpha_t - \varphi_i\right) + E_{pi} \cdot \sin\left(\left(\omega_p - \omega_c\right) \cdot t - \alpha_t + \beta_{pi}\right) - E_c \cdot \sin\left(\beta_c - \varphi_i\right) \cdot \cos\alpha_t, \\ eE_{r1pi}^R &= E_{r1}^R \cdot \sin\left(-\omega_c \cdot t + \beta_{r1} - \alpha_t - \varphi_i\right) + E_{pi} \cdot \sin\left(\left(\omega_p - \omega_c\right) \cdot t - \alpha_t + \beta_{pi}\right) - E_c \cdot \sin\left(\beta_c - \varphi_i\right) \cdot \cos\alpha_t, \\ eE_{spi}^L &= -E_s \cdot \sin\left(\left(\omega_s - \omega_c\right) \cdot t + \beta_s + \alpha_t - \varphi_i\right) - E_{pi} \cdot \sin\left(\left(\omega_p - \omega_c\right) \cdot t + \alpha_t + \beta_{pi}\right) + E_c \cdot \sin\left(\beta_c - \varphi_i\right) \cdot \cos\alpha_t, \\ eE_{spi}^R &= -E_s \cdot \sin\left(\left(\omega_s - \omega_c\right) \cdot t + \beta_s + \alpha_t - \varphi_i\right) - E_{pi} \cdot \sin\left(\left(\omega_p - \omega_c\right) \cdot t + \alpha_t + \beta_{pi}\right) + E_c \cdot \sin\left(\beta_c - \varphi_i\right) \cdot \cos\alpha_t, \end{aligned} \tag{16}$$

where eE_{r2pi}^L, eE_{r1pi}^R, eE_{spi}^L, and eE_{spi}^R, respectively, refer to the equivalent displacements of manufacturing eccentric errors for the ith internal and external meshing pair on the left and right sides of HPGT. E_s, E_{pi}, E_c, E_{r2}^L, and E_{r1}^R, respectively, denote the amplitudes of manufacturing eccentric errors for component g ($g = s$, pi, c, $r2$, and $r1$). β_s, β_{pi}, β_c, β_{r2}, and β_{r1}, respectively, represent the initial phases of manufacturing eccentric errors for component g ($g = s$, pi, c, $r2$, and $r1$). ω_s, ω_p, and ω_c, respectively, mean the angular velocity for component g ($g = s$, p, and c).

4.2. Equivalent Displacements of Tooth Profile Errors. This paper also considers the tooth profile errors, which directly act on the engagement surface of the gear tooth. The tooth

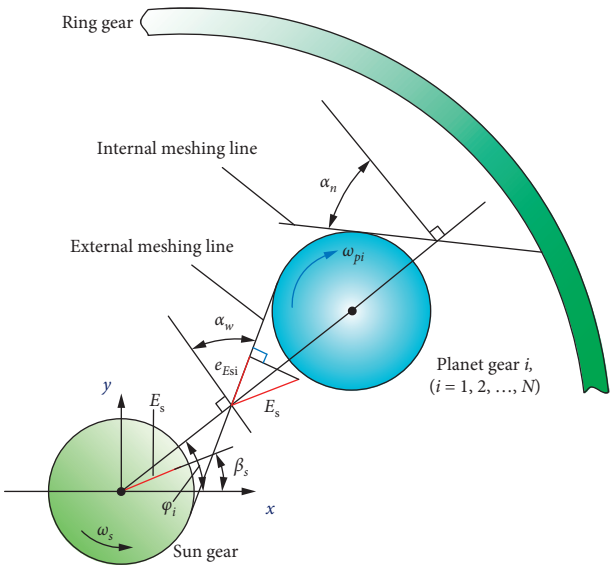

Figure 6: Equivalent meshing error on the line of action in the HPGT system.

engagement is a dynamic interaction between two or more gear teeth. The tooth profile error on the line of action has something to do with the tooth profile errors of the two gears in the gear pair. The profile errors on the meshing tooth surface need to be converted to the meshing line of the gear pair, which are generally performed by using a simple harmonic function according to the meshing frequency. Figure 7 displays the tooth profile error sketch.

The formulas of the tooth profile errors transformed into the external (sun-planet) meshing line are deduced as

$$\begin{aligned} \overline{E}^L_{spi} &= E_{spi} \cdot \sin\left(\omega_m\left(t + \gamma_{si} \cdot T_m\right)\right), \\ \overline{E}^R_{spi} &= E_{spi} \cdot \sin\left(\omega_m\left(t + \gamma_{si} \cdot T_m\right)\right). \end{aligned} \tag{17}$$

Similarly, the computation formulas of tooth profile errors transformed into the internal (ring-planet) meshing line are derived as

$$\begin{aligned} \overline{E}^L_{r2pi} &= E^L_{r2pi} \cdot \sin\left(\omega_m\left(t + \left(\gamma_{si} + \gamma_{sr}\right) \cdot T_m\right)\right), \\ \overline{E}^R_{r1pi} &= E^R_{r1pi} \cdot \sin\left(\omega_m\left(t + \left(\gamma_{ri} + \gamma_{sr}\right) \cdot T_m\right)\right), \end{aligned} \tag{18}$$

where $\overline{E}^L_{spi}, \overline{E}^R_{spi}, \overline{E}^R_{r2pi}$, and $\overline{E}^R_{r1pi}$, respectively, indicate the equivalent displacements of the tooth profile errors for the ith external and internal meshing pair on the left and right sides of the HPGT. E_{spi}, E^L_{r2pi}, and E^R_{r1pi}, respectively, indicate the amplitudes of tooth profile errors for the ith sun-planet pair, ith left and right ring-planet pairs. γ_{si}, γ_{ri}, and γ_{sr}, respectively, denote the ith sun-planet pair phase, ith ring-planet pair phase, and the phase difference between the internal and external mesh. ω_m means the meshing angular frequency. T_m is the meshing cycle in HPGT.

4.3. Multicoupling Manufacturing Errors. In herringbone planetary gears, the excitation of the gear mesh resulting from the gear error is mainly exhibited in the displacement change along the direction of the line of action. The displacement is the superposition of the equivalent displacements of tooth profile error and manufacturing eccentric error of each component. The superpositions of tooth profile error and manufacturing eccentric error on the internal and external meshing lines on the left and right sides are referred to here as multicoupling manufacturing errors, which are denoted by e^L_{spi}, e^R_{spi}, e^L_{r2pi}, and e^R_{r1pi}. The computational formulas of e^L_{spi}, e^R_{spi}, e^L_{r2pi}, and e^R_{r1pi} are given by

$$\begin{cases} e^L_{spi} = eE^L_{spi} + \overline{E}^L_{spi}, e^R_{spi} = eE^R_{spi} + \overline{E}^R_{spi}, \\ e^L_{r2pi} = eE^L_{r2pi} + \overline{E}^L_{r2pi}, e^R_{r1pi} = eE^R_{r1pi} + \overline{E}^R_{r1pi}. \end{cases} \tag{19}$$

Therefore, the HPGT system manufacturing error excitations can be deduced as

$$\begin{aligned} e^L_{spi} &= -E_s \cdot \sin\left(\left(\omega_s - \omega_c\right) \cdot t + \beta_s + \alpha_t - \varphi_i\right) - \left(E_{pi} \cdot \sin\left(\left(\omega_p - \omega_c\right) \cdot t + \alpha_t + \beta_{pi}\right) + E_c \cdot \sin\left(\beta_c - \varphi_i\right) \cdot \cos\alpha_t\right) + E_{spi} \cdot \sin\left(\omega_m\left(t + \gamma_{si} \cdot T_m\right)\right), \\ e^R_{spi} &= -E_s \cdot \sin\left(\left(\omega_s - \omega_c\right) \cdot t + \beta_s + \alpha_t - \varphi_i\right) - \left(E_{pi} \cdot \sin\left(\left(\omega_p - \omega_c\right) \cdot t + \beta_{pi} + \alpha_t\right) + E_c \cdot \sin\left(\beta_c - \varphi_i\right) \cdot \cos\alpha_t\right) + E_{spi} \cdot \sin\left(\omega_m\left(t + \gamma_{si} \cdot T_m\right)\right), \\ e^L_{r2pi} &= E^L_{r2} \cdot \sin\left(-\omega_c \cdot t + \beta_{r2} - \alpha_t - \varphi_i\right) + \left(E_{pi} \cdot \sin\left(\left(\omega_p - \omega_c\right) \cdot t - \alpha_t + \beta_{pi}\right) - E_c \cdot \sin\left(\beta_c - \varphi_i\right) \cdot \cos\alpha_t\right) + E^L_{r2pi} \cdot \sin\left(\omega_m\left(t + \left(\gamma_{si} + \gamma_{sr}\right) \cdot T_m\right)\right), \\ e^R_{r1pi} &= E^R_{r1} \cdot \sin\left(-\omega_c \cdot t + \beta_{r1} - \alpha_t - \varphi_i\right) + \left(E_{pi} \cdot \sin\left(\left(\omega_p - \omega_c\right) \cdot t + \beta_{pi} - \alpha_t\right) - E_c \cdot \sin\left(\beta_c - \varphi_i\right) \cdot \cos\alpha_t\right) + E^R_{r1pi} \cdot \sin\left(\omega_m\left(t + \left(\gamma_{ri} + \gamma_{sr}\right) \cdot T_m\right)\right). \end{aligned} \tag{20}$$

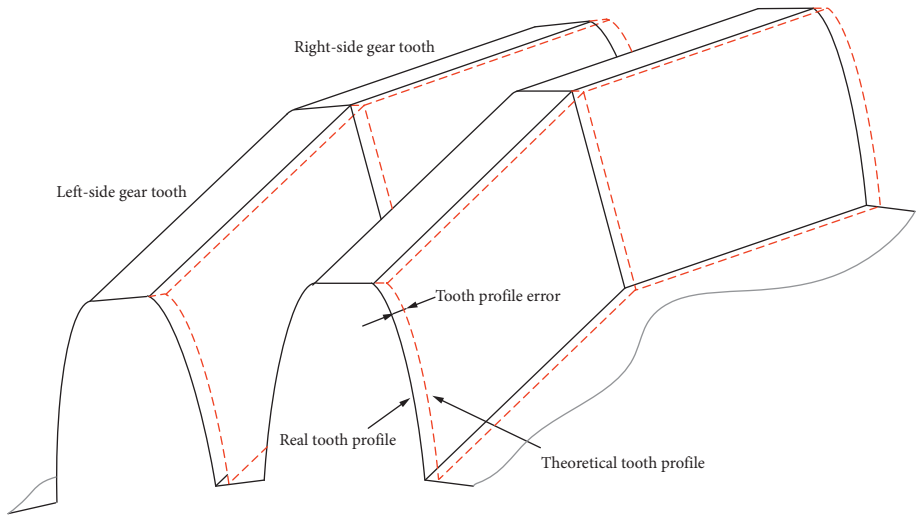

Figure 7: Schematic of tooth profile error.

5. Calculation Approach of the HPGT Load Sharing Coefficients

In a HPGT, due to the influence of elastic deflections and manufacturing errors of each member, the load borne by each planet gear is not equal. The load sharing coefficient is usually utilized to represent the load distribution of the system. The larger the load sharing coefficient is, the more unbalanced the load distribution among different planet gears is. Based on the proposed dynamic load sharing model of HPGT, the load sharing coefficients LSC_{r2pikL}, LSC_{r1pikR}, LSC_{spijL}, and LSC_{spijR} of the ith planet-ring and planet-sun meshes on the left and right sides in each meshing cycle are expressed as

$$\begin{cases} \mathrm{LSC}_{r2pikL} = \dfrac{N \cdot \left(F_{r2pikL}\right)_{\max}}{\sum_{i=1}^{N} \left(F_{r2pikL}\right)_{\max}}, \\ \mathrm{LSC}_{r1pikR} = \dfrac{N \cdot \left(F_{r1pikR}\right)_{\max}}{\sum_{i=1}^{N} \left(F_{r1pikR}\right)_{\max}}, \\ \mathrm{LSC}_{spijL} = \dfrac{N \cdot \left(F_{spijL}\right)_{\max}}{\sum_{i=1}^{N} \left(F_{spijL}\right)_{\max}}, \\ \mathrm{LSC}_{spijR} = \dfrac{N \cdot \left(F_{spijR}\right)_{\max}}{\sum_{i=1}^{N} \left(F_{spijR}\right)_{\max}}, \end{cases} \tag{21}$$

where $i = 1, 2, \ldots, N$. j and k are the meshing cycle numbers. N is the planet number. F indicates the dynamic meshing force in the meshing cycle which can be calculated by equation 4.

The load sharing coefficients LSC_{r2piL}, LSC_{r1piR}, LSC_{spiL}, and LSC_{spiR} of the ith internal and external meshes on the left and right sides of HPGT in a system period can be obtained as

$$\begin{cases} \mathrm{LSC}_{r2piL} = 1 + \left|\mathrm{LSC}_{r2pikL} - 1\right|_{\max}, \\ \mathrm{LSC}_{r1piR} = 1 + \left|\mathrm{LSC}_{r1pikR} - 1\right|_{\max}, \\ \mathrm{LSC}_{spiL} = 1 + \left|\mathrm{LSC}_{spijL} - 1\right|_{\max}, \\ \mathrm{LSC}_{spiR} = 1 + \left|\mathrm{LSC}_{spijR} - 1\right|_{\max}. \end{cases} \tag{22}$$

The system load sharing coefficients LSC_{r2pL}, LSC_{r1pR}, LSC_{spL}, and LSC_{spR} of the internal and external meshes on the left and right sides of herringbone gear in a system cycle are written as

$$\begin{cases} \mathrm{LSC}_{r2pL} = \max\limits_{1 \le i \le N} \left(\mathrm{LSC}_{r2piL}\right), \\ \mathrm{LSC}_{r1pR} = \max\limits_{1 \le i \le N} \left(\mathrm{LSC}_{r1piR}\right), \\ \mathrm{LSC}_{spL} = \max\limits_{1 \le i \le N} \left(\mathrm{LSC}_{spiL}\right), \\ \mathrm{LSC}_{spR} = \max\limits_{1 \le i \le N} \left(\mathrm{LSC}_{spiR}\right). \end{cases} \tag{23}$$

Therefore, the load sharing coefficient LSC in a system period is denoted as

$$\mathrm{LSC} = \max\left(\mathrm{LSC}_{r2pL}, \mathrm{LSC}_{r1pR}, \mathrm{LSC}_{spL}, \mathrm{LSC}_{spR}\right). \tag{24}$$

6. Numerical Simulations

In this paper, the HPGT system with three planet gears as demonstrated in Figure 1 is numerically simulated and analyzed. The basic parameters of the set are given in Tables 1 and 2.

6.1. Influence of Manufacturing Errors on HPGT Load Sharing. In order to investigate the impacts of manufacturing errors such as the carrier eccentric error on the HPGT system load sharing coefficient, it is assumed that only the carrier eccentric error E_c is variable, while the tooth profile errors and the eccentric errors of other components are constant.

Table 1: Parameters of the HPGT system.

Subject	Carrier	Planet	Sun	Left ring	Right ring
Tooth number	—	17	23	57	57
Helix angle (deg.)	—	25	25	25	25
Tooth width (mm)	—	360	360	170	170
Normal pressure angle (deg.)	—	20	20	20	20
Mass (kg)	5091	525	750	450	450
Equivalent moment of inertia J/r^2 (kg)	5724	420	663	546	546
Material			20CrMnMo		
Input torque (kN·m)			100		
Input speed (r/min)			100		

Table 2: Stiffness parameters of the HPGT system.

Subject (N/m)	u-direction	x-direction	y-direction	z-direction
Carrier	—	1e9	1e9	1e9
Planet	—	1e9	1e9	1e9
Sun	—	1e9	1e9	1e9
Left ring	1e10	1e10	1e10	1e10
Right ring	1e10	1e10	1e10	1e10

Figure 8 exhibits a schematic diagram of the planet-carrier eccentric error E_c. Figure 9 shows the variation of the system load sharing coefficient LSC with the carrier eccentric error E_c in different floating configurations when manufacturing errors of the other elements are constant as 20 μm. In Figure 8, α represents the result for the model without floating, γ is the result for the model with the sun gear float, and $\triangle$ indicates the result for the model with the floating sun gear and carrier. From Figure 9, it can be seen that the carrier eccentric error E_c has prominent effects on the load sharing behavior of the HPGT system. That is, the load distribution amongst different planet gears becomes worse with the increase of error E_c. Meanwhile, it is also found that the floating configurations of the HPGT have an appreciable impact on the load sharing performance. For the model with nonfloating, the load sharing coefficient LSC is larger, meaning at this time, there exists a more serious load distribution imbalance amongst different planet gears in HPGT. In contrast with the result for the model with the single floating as displayed by the black solid line γ in Figure 9, the combined floating is better. In other words, the load distribution among different planet gears is more even and balanced under the combined floating configurations as exhibited by the red double dot-dashed line $\triangle$ in Figure 9. In short, the planet-carrier eccentric error E_c and floating configurations significantly affect the HPGT system load sharing performance, and as the planet-carrier eccentric error E_c goes up, the HPGT system load sharing coefficient LSC becomes larger. Floating can reduce the HPGT load sharing coefficient; that is, when the floating form is adopted, the load distribution amongst different planet gears will become more uniform. Moreover, the combination of floating is better than the single floating, and this shows a good agreement with Ren's study [11].

Figure 10 illustrates the variation of the load sharing coefficients of each planet gear of the external mesh with the meshing time under multiple manufacturing errors, where

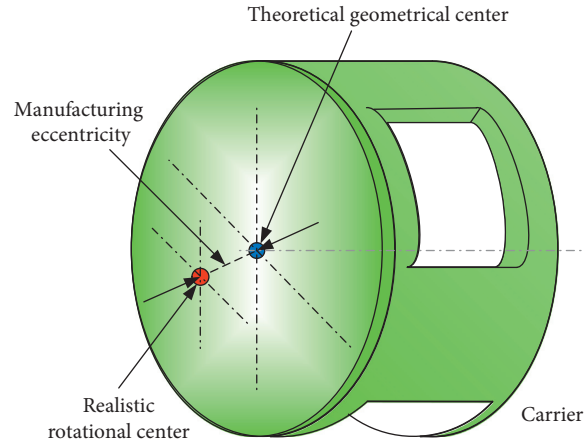

Figure 8: Schematic diagram of the planet-carrier eccentric error.

$\mathrm{LSP}_{spiL(R)}$ ($i = 1, 2, \ldots, N$) denotes the ith planet-gear load sharing coefficient of the external mesh at the left (right) side as described in formula (22) and N is the planet number; here $N = 3$. The tooth profile errors and eccentric errors of each component are assumed to be 20 μm. It can be observed from Figure 10 that the load sharing coefficient of each planet gear in HPGT shows a certain periodic change. This is mainly because the error excitation is a simple harmonic function. By comparing Figures 10(a) and Figure 10(b), it can be found that the change curves of the load sharing coefficients of the corresponding planet gear i of the left-side and right-side external mesh are the same. It can also be seen that, under multiple manufacturing errors, the example HPGT system load sharing coefficient is 1.15.

In this subsection, it is assumed that only a single manufacturing error such as the sun-gear eccentric error E_s or the planet-gear eccentric error E_{p1} exists, while the other error values are zero. Figure 11 demonstrates the variation of the load sharing coefficient of each planet gear at the right-

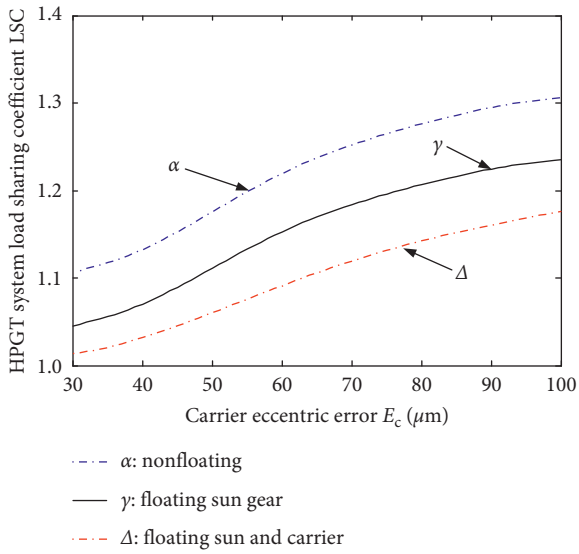

Figure 9: Relationships between the HPGT system load sharing coefficient (LSC) and the planet-carrier eccentric error E_c in different floating configurations.

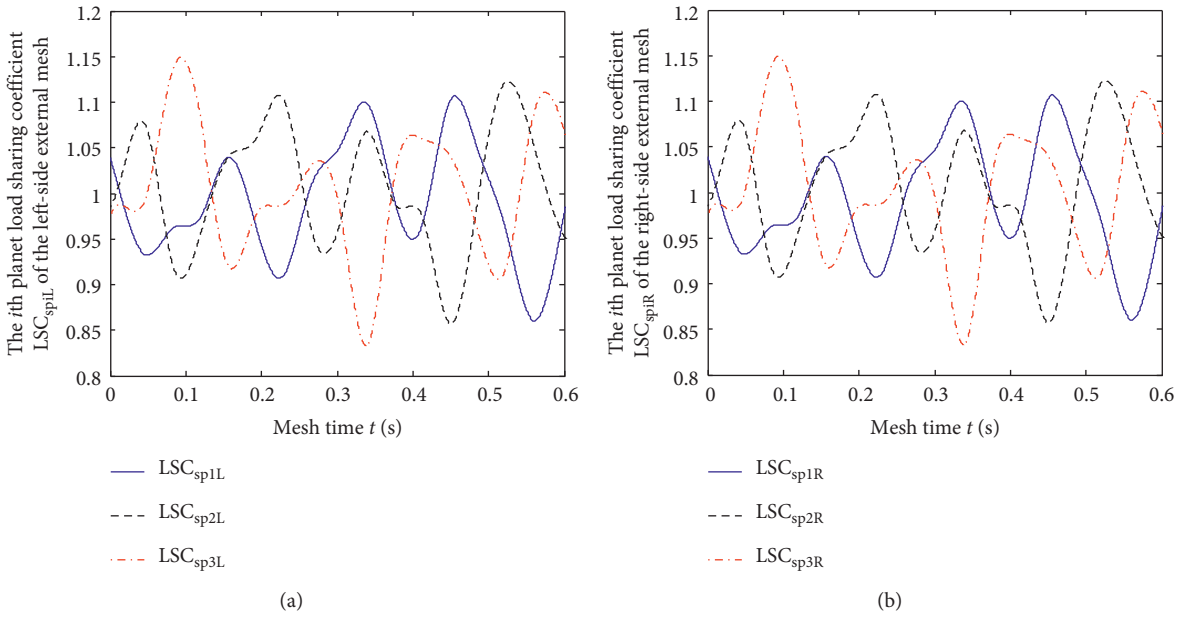

Figure 10: The variation of the planet-gear load sharing coefficients under multiple manufacturing errors. (a) The left-side external mesh LSC_{spiL}. (b) The right-side external mesh LSC_{spiR}.

side external mesh in the HPGT system with the meshing time, where (a) and (b) are the results from the model with the sun-gear eccentric error $E_s = 20\,\mu$m and the planet-gear eccentric error $E_{p1} = 20\,\mu$m, respectively. From Figure 11, it can be observed that, in these two models with the sun-gear eccentricity and planet-gear eccentricity, the planet-gear load sharing coefficients of the right-side external mesh fluctuate periodically with the meshing time. The system load sharing coefficient can be obtained by the maximum values in each planet-gear load sharing coefficient changing curve. The HPGT system load sharing coefficients from the model with the sun-gear eccentricity $E_s = 20\,\mu$m and the planet-gear eccentricity $E_{p1} = 20\,\mu$m are 1.10 and 1.043, respectively. This shows, in the HPGT system, the load distribution situation among different planet gears under the sun-gear eccentric error excitation $E_s = 20\,\mu$m is even worse and more uneven than that under the planet-gear eccentric error excitation $E_{p1} = 20\,\mu$m. This is possible because the example HPGT system is more sensitive to the sun-gear eccentric error excitation. By comparing Figures 10 and 11, it can be found that the example HPGT system load sharing coefficient LSC under multiple manufacturing errors shown in Figure 10 is larger than that under a certain single error shown in Figure 11. The manufacturing error impact on the load sharing coefficient exhibits a cumulative effect, and this has a good agreement with Ren's investigation [12].

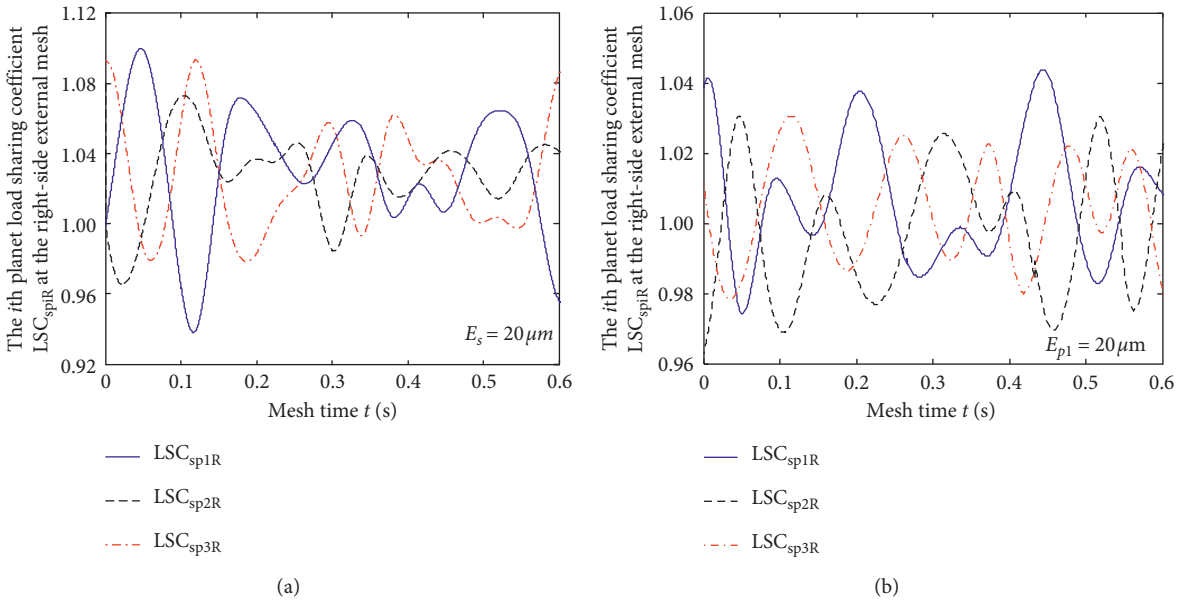

FIGURE 11: The variation of the planet-gear load sharing coefficients LSC$_{spiR}$ of the right-side external mesh in the HPGT. (a) The model with the sun-gear eccentric error $E_s = 20\,\mu$m. (b) The model with the planet-gear eccentric error $E_{p1} = 20\,\mu$m.

6.2. Influence of System Support Stiffness on HPGT Load Sharing. To investigate the effects of the support stiffness of the central member (i.e., sun gear, ring gears, and carrier) on the HPGT system load sharing coefficient LSC, it is assumed that only the support stiffness of the sun gear, ring gears, and carrier is changed while the other parameters are fixed. Figure 12 demonstrates the variation of system load sharing coefficient LSC with the support stiffness of the center member, where the blue solid line α denotes the variation of the carrier support stiffness k_c, the red double dot-dash line β denotes the variation of ring gear support stiffness k_r, and the black dashed line γ denotes the variation of sun gear support stiffness k_s. From Figure 12, it is found that the support stiffness of the central member, such as the sun gear support stiffness k_s, the ring-gear support stiffness k_r , and the carrier support stiffness k_c, significantly affects the load sharing performance. When the supporting stiffness of the central component ranges from 0 to 1.5×10^{10} N/m and gradually increases, the HPGT system load sharing coefficient LSC is very sensitive to the supporting stiffness of the central component in the initial stage and increases rapidly with an increase in the supporting stiffness of the central component. When the supporting stiffness of the central member is greater than 1.5×10^{10} N/m and increases further, the system load sharing coefficient increases at a slow pace. After the support stiffness of the central member increases to a certain extent, the system load sharing coefficient changes insignificantly and approaches a fixed value. In addition, when the sun gear, carrier, and ring gear have the same support stiffness value, the system load sharing coefficient LSC under the variation of the sun gear support stiffness k_s is the smallest and is the largest under the carrier support stiffness k_c, while it is in-between under the ring gear support stiffness k_r. In other words, when the sun gear, ring gear, and carrier have the same support stiffness value, the floating of the sun gear gives the best results and the floating of the carrier is the worst. This may be due to the fact that the sun gear inertia is the smallest, and the floating is more sensitive and easier to achieve.

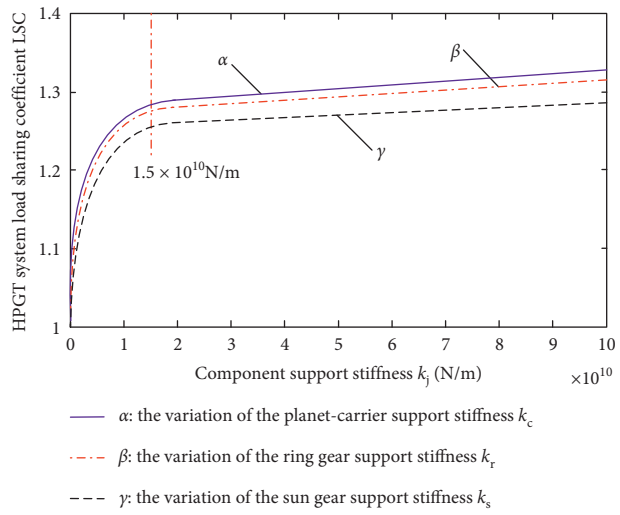

FIGURE 12: Relationships between the support stiffness for the central element in the HPGT and the system load sharing coefficient.

7. Verifications of Theoretical Results

In order to verify the validity of theoretical calculation in the present study, the approaches of comparing the obtained research results in the paper with the existing literature are mainly adopted to validate the correctness of the proposed model and method. Influence curves of carrier eccentricity *Ec* on the HPGT LSC shown in Figure 9 in this research have

a similar tendency and changing law with Mo's investigation in [19], and both of them show a good agreement. The LSC curves of the left and right sides shown in Figure 10 are the same, which is consistent with Mo's study in [19]. Moreover, all the variation curves of LSC of each planet gear in Figures 10 and 11 in the present investigation exhibit the periodically changing trend, and just these are relatively consistent with [19, 20]. Meanwhile, from Figures 10 and 11, it is obvious that the HPGT system LSC under multicoupling errors is larger than that under single error, which is consistent with [19]. As exhibited in Figure 12, the variation tendencies and laws of the system LSC curves with the central member (i.e., sun, ring, and carrier) are consistent with [21].

In summary, comparing the theoretical calculation results in the study with the existing literature, both of them are in a good agreement. In other words, the reliability and correctness of theoretical calculation are validated.

8. Conclusions

Based on the actual structure feature of herringbone gears and by considering multicoupling manufacturing errors, time-dependent meshing stiffness, bearing deformation, and gyroscopic effect, a refined bending-torsional-axial coupled dynamic model for HPGT has been developed to study the load sharing performance. The influences of manufacturing errors and system support stiffness on dynamic load sharing behavior were numerically investigated. The main conclusions are summarised as follows:

(1) Manufacturing errors such as the planet-carrier eccentric error E_c and component floating have palpable influences on the load sharing behavior of the HPGT system. The load sharing coefficient increases significantly with the increase of manufacturing errors. The system load sharing coefficient is significantly smaller when using the component floating, and the load distribution among planet gears tends to be more uniform under a combined floating configuration. Hence, adopting component floating and lessening manufacturing errors exert a vital role in the load sharing of the HPGT system. And the HPGT load sharing coefficient when the errors act in common is larger than that when the error acts alone. The influence of the error on the load sharing coefficient has a cumulative effect.

(2) The support stiffness of the central member noticeably affects the HPGT load sharing behavior. When the support stiffness of the central member is gradually increased, the load sharing coefficient is also increased in the initial stage. As the support stiffness of the central component is further increased, the increase of the load sharing coefficient becomes slower. After the support stiffness increases to a certain extent, the system load sharing coefficient LSC no longer changes significantly and tends to be a fixed value. This will provide a theoretical foundation for reasonably selecting the support stiffness of the central component.

Data Availability

The data used to support the findings of this study are included within the article.

Conflicts of Interest

The authors declare no conflicts of interest regarding the publication of this article.

Acknowledgments

The projects supported by the Science and Technology Research Project from Henan Province (Grant nos. 202102210085 and 172102210056), the Open Funding of Henan Key Laboratory of Intelligent Manufacturing of Mechanical Equipment (Grant no. IM201912), and the Doctoral Science Research Foundation of Zhengzhou University of Light Industry (Grant no. 2015BSJJ030) are acknowledged.

References

[1] F. Ren, D. Qin, T. C. Lim, and S. Lyu, "Study on dynamic characteristics and load sharing of a herringbone planetary gear with manufacturing errors," *International Journal of Precision Engineering and Manufacturing*, vol. 15, no. 9, pp. 1925–1934, 2014.

[2] J. Lin and R. G. Parker, "Planetary gear parametric instability caused by mesh stiffness variation," *Journal of Sound and Vibration*, vol. 249, no. 1, pp. 129–145, 2002.

[3] J. Lin and R. G. Parker, "Analytical characterization of the unique properties of planetary gear free vibration," *Journal of Vibration and Acoustics*, vol. 121, no. 3, pp. 316–321, 1999.

[4] M. Zhao and J. C. Ji, "Nonlinear torsional vibrations of a wind turbine gearbox," *Applied Mathematical Modelling*, vol. 39, no. 16, pp. 4928–4950, 2015.

[5] L. Zhang and R. Zhu, "Impact of meshing phase on load sharing for herringbone planetary train," *Journal of Mechanical Engineering*, vol. 54, no. 11, pp. 129–140, 2018.

[6] S. Mo, Y. Zhang, Q. Wu, S. Matsumura, and H. Houjoh, "Load sharing behavior analysis method of wind turbine gearbox in consideration of multiple-errors," *Renewable Energy*, vol. 97, pp. 481–491, 2016.

[7] A. Singh, "Load sharing behavior in epicyclic gears: physical explanation and generalized formulation," *Mechanism and Machine Theory*, vol. 45, no. 3, pp. 511–530, 2010.

[8] A. Singh, "Application of a system level model to study the planetary load sharing behavior," *Journal of Mechanical Design*, vol. 127, no. 3, pp. 469–476, 2005.

[9] H. Ligata, A. Kahraman, and A. Singh, "An experimental study of the influence of manufacturing errors on the planetary gear stresses and planet load sharing," *Journal of Mechanical Design*, vol. 130, no. 4, Article ID 041701, 2008.

[10] A. Bodas and A. Kahraman, "Influence of carrier and gear manufacturing errors on the static load sharing behavior of planetary gear sets," *JSME International Journal Series C*, vol. 47, no. 3, pp. 908–915, 2004.

[11] C. Zhu, X. Xu, T. C. Lim, X. Du, and M. Liu, "Effect of flexible pin on the dynamic behaviors of wind turbine planetary gear

drives," *Proceedings of the Institution of Mechanical Engineers-Part C: Journal of Mechanical Engineering Science*, vol. 227, no. 1, pp. 74–86, 2013.

[12] F. Ren, G. Luo, G. Shi, X. Wu, and N. Wang, "Influence of manufacturing errors on dynamic floating characteristics for herringbone planetary gears," *Nonlinear Dynamics*, vol. 93, no. 2, pp. 361–372, 2018.

[13] F. Ren, A. Li, G. Shi, X. Wu, and N. Wang, "The effects of the planet-gear manufacturing eccentric errors on the dynamic properties for herringbone planetary gears," *Applied Sciences*, vol. 10, no. 3, p. 1060, 2020.

[14] M. Li, L. Xie, and L. Ding, "Load sharing analysis and reliability prediction for planetary gear train of helicopter," *Mechanism and Machine Theory*, vol. 115, pp. 97–113, 2017.

[15] M. R. Kang and A. Kahraman, "An experimental and theoretical study of the dynamic behavior of double-helical gear sets," *Journal of Sound and Vibration*, vol. 350, pp. 11–29, 2015.

[16] P. Sondkar and A. Kahraman, "A dynamic model of a double-helical planetary gear set," *Mechanism and Machine Theory*, vol. 70, pp. 157–174, 2013.

[17] L. Zhang, Y. Wang, K. Wu, and R. Sheng, "Three-dimensional modeling and structured vibration modes of two-stage helical planetary gears used in cranes," *Shock and Vibration*, vol. 2017, Article ID 9864959, 18 pages, 2017.

[18] F. Guo, Z. Fang, X. Zhang, and Y. Cui, "Influence of the eccentric error of star gear on the bifurcation properties of herringbone star gear transmission with floating sun gear," *Shock and Vibration*, vol. 2018, Article ID 6014570, 32 pages, 2018.

[19] S. Mo, T. Zhang, G. Jin, Z. Feng, J. Gong, and S. Zhu, "Influence mechanism of multi-coupling error on the load sharing characteristics of herringbone gear planetary transmission system," *Proceedings of the Institution of Mechanical Engineers-Part K: Journal of Multi-Body Dynamics*, vol. 233, no. 4, pp. 792–816, 2019.

[20] S. Mo, T. Zhang, G. Jin, X. Cai, and H. Gao, "Analytical investigation on load sharing characteristics of herringbone planetary gear train with flexible support and floating sun gear," *Mechanism and Machine Theory*, vol. 144, Article ID 103670, 2020.

[21] L. Zhang, *The Study on load sharing properties and optimazition of large scale wind turbine gearbox*, PhD thesis, Mechanical Science Research Institute, Durgapur, India, 2009.